Materials and Design 187 (2020) 108394

Contents lists available at ScienceDirect

Materials and Design

journal homepage: www.elsevier.com/locate/matdes

Microstructure evolution and mechanical properties of new die-cast Al-Si-Mg-Mn alloys

Qing Cai, Chamini L. Mendis, Isaac T.H. Chang *, Zhongyun Fan

Brunel Centre for Advanced Solidification Technology (BCAST), Brunel University London, Uxbridge UB8 3PH, UK

HIGHLIGHTS

- CALPHAD modelling was used to predict various volume fraction of eutectic mixture based on Al-Si-Mg-Mn system.
- Ultrafine binary (Al + Mg_2Si) and quaternary (Si + α-Al + Mg_2Si + π-AlFeMnSiMg) eutectic were achieved in the die-cast alloys.
- The ultrafine eutectic mixture and fine α-AlFeMnSi particles result in high strength of the alloys.
- The higher volume fraction of eutectic mixture decreases the elongation but enhances the yield strength.

GRAPHICAL ABSTRACT

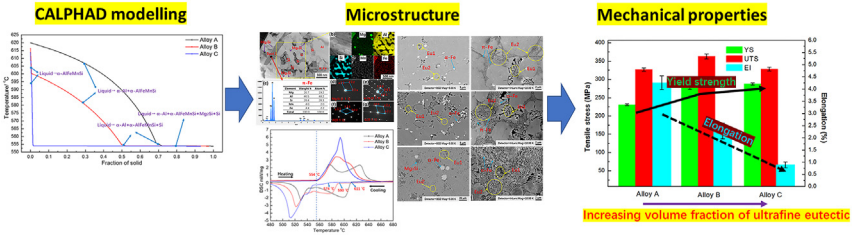

ARTICLE INFO

Article history:
Received 31 August 2019
Received in revised form 28 November 2019
Accepted 28 November 2019
Available online 29 November 2019

Keywords:
Aluminium alloys
CALPHAD
High pressure die casting
Microstructure
Mechanical properties

ABSTRACT

The microstructure evolution and mechanical properties of recently developed die-cast Al-Si-Mg-Mn alloys were investigated. CALPHAD modelling, based on the thermodynamic database, was carried out to design Al-Si-Mg-Mn alloys with different solid fractions of the eutectic mixture. Experimental results confirmed that the new Al-Si-Mg-Mn alloys have excellent yield strength of 230–280 MPa, ultimate tensile strength of 340–370 MPa and elongation to fracture of 2.3–4.3% from the standard tensile samples under as-cast condition. The as-cast microstructure consists of α-Al, α-AlFeMnSi, binary eutectic (Al + Mg_2Si) and ultrafine quaternary eutectic (Si + α-Al + Mg_2Si + π-AlFeMnSiMg). The high strength is induced by the formation of multi-scale eutectic mixtures and fine α-AlFeMnSi particles. The newly designed Al-Si-Mg-Mn alloys offer 20–50% increase in yield strength with good ductility, as compared with the commercially available die-cast aluminium alloys.

© 2019 Published by Elsevier Ltd. This is an open access article under the CC BY-NC-ND license (http://creativecommons.org/licenses/by-nc-nd/4.0/).

1. Introduction

High-pressure die casting (HPDC) has been widely used for the production of automotive components with many advantages including good surface finish, high dimensional accuracy and excellent mechanical properties [1,2]. The application of die-cast aluminium alloys has increased considerably in the past ten years to replace steel parts due to its lightweight for improved fuel efficiency in automotive vehicles. For many decades, great efforts have been made on the development of die-cast aluminium alloys with enhanced mechanical properties. The registered die-cast aluminium alloys are mainly based on Al—Si, Al-Si-Cu, Al-Si-Mg, Al-Si-Cu-Mg and Al—Mg systems [3]. The mechanical properties of commercially available die-cast alloys are

* Corresponding author.
E-mail address: isaac.chang@brunel.ac.uk (I.T.H. Chang).

https://doi.org/10.1016/j.matdes.2019.108394
0264-1275/© 2019 Published by Elsevier Ltd. This is an open access article under the CC BY-NC-ND license (http://creativecommons.org/licenses/by-nc-nd/4.0/).

Table 1
Mechanical properties of commercial aluminium alloys for HPDC [15,16].

Alloy	Alloy system	Tensile strength /MPa	Yield strength /MPa	Shear strength /MPa	Elongation /%in 50 mm
413	Al-Si	295	145	170	2.5
383	Al-Si-Cu	310	150	–	3.5
B390	Al-Si-Cu-Mg	317	250	–	1
A360	Al-Si-Mg	317	170	180	3.5–5
A380	Al-Si-Cu	325	160	185	3.5–4.5
383/384	Al-Si-Cu	310–330	150–165	–	2.5–3.5
A413	Al-Si	290	130	170	3.5
361	Al-Si-Mg	250–290	120–150	–	5–7
A360	Al-Si-Mg	270–300	140–160	–	3–6
516	Al-Mg	290–315	170–190	–	10
518	Al-Mg	310	190	–	5–8

listed in Table 1. They exhibit yield strength and elongation to fracture of approximately 120–190 MPa and 2–8%, respectively. In order to improve the mechanical properties, alloying elements such as Cu, Mn, Zn or Mg have been added into the die-cast aluminium alloys, resulting in the formation of AlMgZn, Al_2Cu, AlMn or $CuZn_4$ intermetallics that contribute to the strengthening mechanism. In addition, solid solution strengthening and precipitation hardening are also responsible for enhanced mechanical properties of these alloys. Zhang et al. developed Al-5 Mg-0.6Mn (wt%) die-cast alloy that has a yield strength of ~212 MPa [4]. The Al-8.8Si-1.7Cu-0.4 Mg-0.5Mn (wt%) with a yield strength of about 200 MPa and ultimate tensile strength 370 MPa was first reported by Dong et al. [5]. Furthermore, the Al-11 Mg-3.5Zn-3Si (wt%) die-cast alloy was developed by Ji et al. [6] and it has a yield strength of about 250 MPa, an ultimate tensile strength of 350 MPa and elongation to fracture of 2.5% under as-cast condition. Further strength improvement of the die-cast alloys can be obtained by conventional processing methods including solution and artificial ageing treatments. However, heat treatment of die-cast alloys at a high temperature (e.g. 540 °C) can cause unacceptable surface blistering and dimensional instability, resulting from entrapment of gas [7]. It is reported that the addition of Mn is essential, due to its prohibition of die soldering and the suppression of β-Fe phases [8]. However, besides the improvement of the mechanical properties, the addition of Cu or Zn increases not only the density of the alloys but also the cost of these alloys. In addition, it is detrimental to hot tearing or reduction of corrosion resistance of Al—Si cast alloys [9–11].

In recent years, the ultrafine eutectic and hypoeutectic multicomponent alloys with bimodal/multi-modal microstructure had drawn considerable attention due to the benefit of the ultrafine eutectic structure to improve the plasticity and damage tolerance [12]. The development of ultrafine eutectic alloys has been reported on a limited number of alloy systems. The multicomponent TiNbCoCuAl alloy with an ultrafine eutectic microstructure was developed by Okulov et al. [13]. Such multicomponent alloy exhibits a combination of good strength and high ductility. This is due to the presence of ultrafine eutectic microstructure, together with specific orientation relationship between eutectic phases that can inhibit the propagation of dislocations. It is believed that the high strength property of this alloy is due to the restricted mobility of dislocation by the nano/ultrafine eutectic mixture, while large ductility property is due to the strain accommodation or stress relaxation reported by Kim et al. [14]. For die-cast aluminium

Table 2
Measured compositions of Al-Si-Mg-Mn die-cast alloys.

Alloy	Alloy composition (wt%)				
	Al	Si	Mg	Mn	Fe
A	Balance	5.22	2.35	0.48	0.16
B	Balance	7.48	3.55	0.52	0.18
C	Balance	13.17	5.81	0.47	0.20

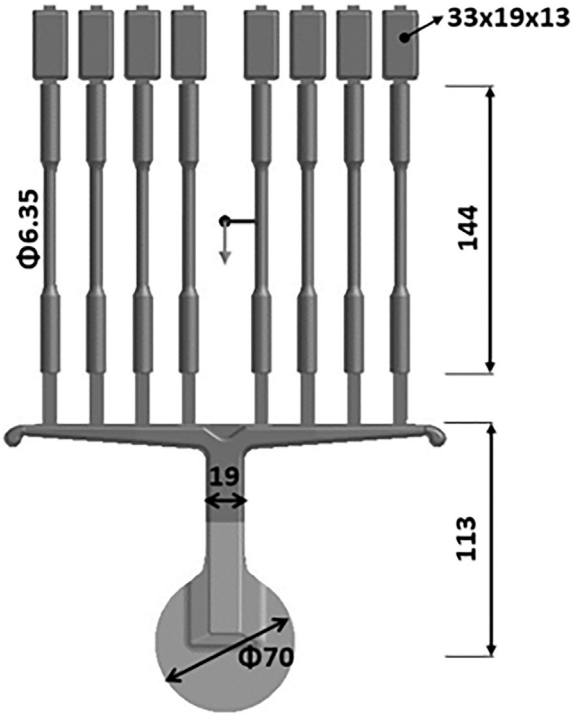

Fig. 1. The dimension of die casting with overflow and biscuit.

alloys, there is still a challenge to improve the yield strength and fracture elongation to a level above 200 MPa and 4%, respectively. The development of multicomponent eutectic systems for die-cast aluminium alloys provides a potential route to enhance the yield strength beyond 200 MPa with reasonable elongation to fracture.

The purpose of current work is to design multicomponent aluminium based die-cast alloys with yield strength in excess of 200 MPa without the addition of Cu or Zn. Since ternary Al-Si-Mg alloys, such as A356, A357 and A360, exhibit good mechanical properties, age hardening response, excellent castability, low density and good weldability [17,18]. Therefore, the quaternary Al-Si-Mg-Mn eutectic system was selected for the development of high strength die-cast aluminium alloys using schematic studies of the microstructural evolution and tensile mechanical properties.

2. Experiment

The starting materials used in the present study were elemental Al and Mg with commercial purity (99.9%) and master alloys of Al-50wt

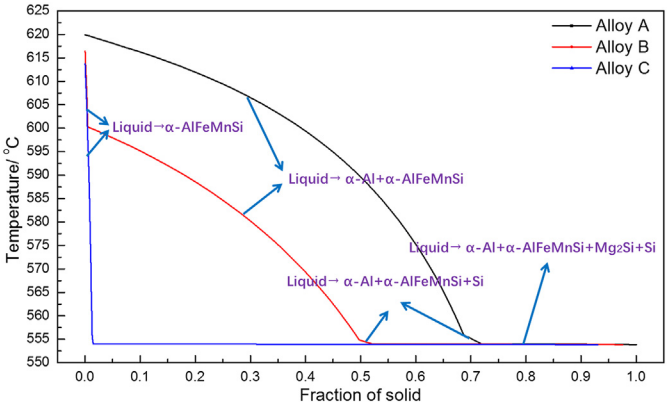

Fig. 2. Solidification path of Al-Si-Mg-Mn alloys calculated by the CALPHAD software Pandat 8.5.

Table 3
The calculated content of elements in the Al-Si-Mg-Mn die-cast alloys.

Alloy	Volume fraction of eutectic mixture	Alloy composition (wt%)				
		Al	Si	Mg	Mn	Fe
A	0.3	Balance	5.16	2.05	0.5	~0.15
B	0.5	Balance	7.66	3.05	0.5	~0.15
C	1.0	Balance	13.9	5.55	0.5	~0.15

%Si and Al-20wt%Mn. A 6 kg melt of the starting materials apart from elemental Mg, was prepared each time in a clay-graphite crucible with an electric resistance furnace. The melt temperature was maintained at 720 ± 5 °C. Pure Mg ingots preheated to a temperature of 200 °C were carefully added to the melt. After half-hour homogenisation, argon gas was introduced into the melt via a commercial rotatory degasser at 500 rpm for 5 min. The melt was then covered by commercial granular flux, following by further homogenisation for about 15 min. Optical mass spectroscopy was used to determine the actual compositions of as-cast alloys and these measured compositions are listed in Table 2.

The 4500 kN HPDC machine was used for making standard tensile testing samples. The melt was dosed and poured into the shot sleeve with a temperature 60 °C above the liquids temperature, as measured by a K-type thermocouple. For each HPDC run, the total mass of melt was maintained at about 750 g with an initial injection speed of ~2.3 m/s and gate speed of ~62 m/s. A designed tensile testing mould was used to cast eight ASTM standard samples with a diameter of Φ6.35 mm and a gauge length of 50 mm. The dimension of the die casting, including overflow and biscuit, is shown in Fig. 1. During casting, the mould was pre-heated by mineral oil to a temperature of 250 °C. The casting samples were tensile tested after being left at ambient condition for more than one day.

Samples for microstructural evaluation were taken near the centre region from the middle of φ6.35 mm tensile rods. After cold mounting, grinding and polishing, the samples were examined using a Zeiss optical microscope with quantitative metallography. The volume fraction was determined from more than five different areas, ranging from the edge to the centre of each sample using ImageJ software. The samples were etched for 2 s by 0.5% HF acid for scanning electron microscopy (SEM) characterisation using a Zeiss Supera 35 FEG SEM equipped with the energy dispersive spectroscopy (EDX). The electron backscatter diffraction (EBSD) with a step size of 0.4 μm was used for grain size measurement. The sample was electrolytically polished with a solution of nitric acid and methyl alcohol (1:3) at a temperature of −30 °C. OIM TSL software was used for the statistic analysis of grain size. The X-ray diffraction (XRD) sample was prepared from the vertical section of the Φ6.35 mm rod. A Bruker D8 Advance X-ray diffractometer with Cu X-Ray radiation and Ni filter operated at a voltage of 40 kV and a current of 40 mA was used to generate X-ray line profiles on each sample for phase identification. Transmission electron microscopy (TEM) specimens were prepared by milling the sample to a thickness of around 80 nm and applying the lift-out technique in a Zeiss Auriga cross beam focused ion beam (FIB) using Cu grid with Pt deposition. A JEOL 2100F TEM was used to study the refined microstructure. The melting temperature and heat of fusion of Al-Si-Mg-Mn alloys were determined using a Netzsch 404F1 differential scanning calorimetry (DSC) instrument operated at a heating rate of 20 K/min, in a dynamic flow of Ar at a flow rate of 50 ml/min.

The ASTM B557 standard tensile testing was carried out on an Instron 5500 machine. The extensometer with 50 mm gauge length was used and the testing rate was set at 1 mm/min. The testing data were obtained from at least 6 test specimens from each alloy.

3. Results

3.1. CALPHAD of the multicomponent Al-Si-Mg-Mn system

The eutectic reaction (L → α-Al + Mg_2Si + Si) in Al-Si-Mg ternary system at aluminium corner was calculated with Pandat 8.5 software to be Al13.9%Si5.55%Mg (wt%). Based on Al-Si-Mg eutectic composition, the hypo-eutectic Al-Si-Mg alloys with 30% and 50% volume percentages of the eutectic mixture were calculated. The excess Mn was introduced to prevent die soldering and the formation of Mn contained strengthening phases. Fe is considered as an impurity in HPDC. Hence, the predicted solidification paths of both eutectic and hypo-eutectic compositions in Al-Si-Mg-Mn system with Fe impurity based on Scheil description, are shown in Fig. 2. The calculated compositions of Al-Si-Mg-Mn alloys were listed in Table 3, which are named as alloy A, alloy B and alloy C, respectively.

The solid fraction of eutectic mixture changes from ~0.3 to ~1 with different amount of Si and Mg. All three alloys have the same final quaternary eutectic reaction L → α-Al + α-AlFeMnSi+Mg_2Si + Si at the same eutectic temperature of ~554 °C. L → α-AlFeMnSi with a solid fraction of about 0.011 forms in alloy B prior to the reaction of L → α-AlFeMnSi+α-Al, while only one reaction (L → α-AlFeMnSi+α-Al) is found before eutectic reaction in alloy A. Both alloy B and alloy A have same ternary eutectic reaction L → α-Al + α-AlFeMnSi +Si with a

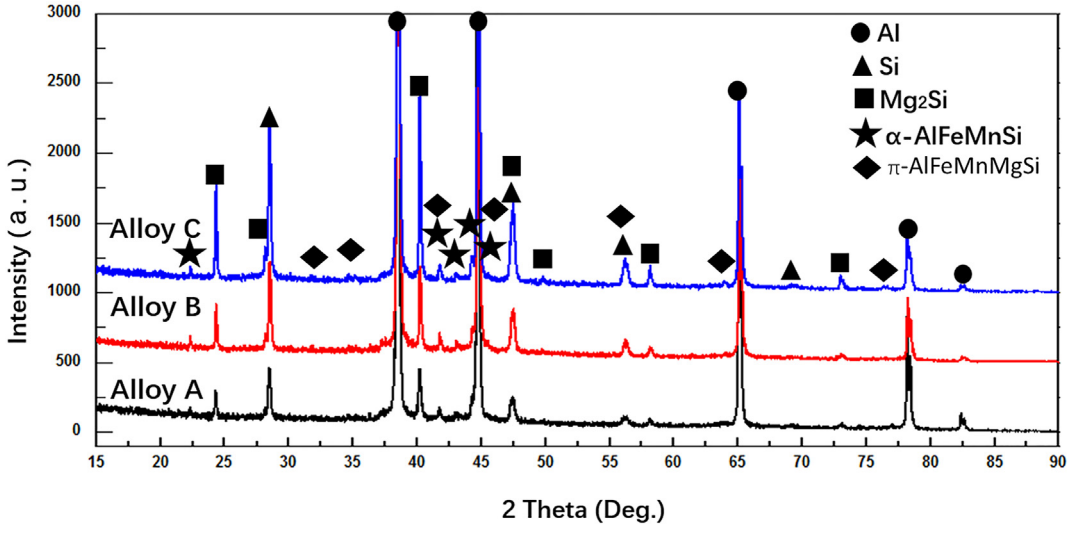

Fig. 3. The XRD spectrum of the Al-Si-Mg-Mn alloys.

solid fraction of approximate 0.03, followed by the final quaternary eutectic reaction L → α-Al + α-AlFeMnSi + Si + Mg_2Si.

3.2. Microstructure

3.2.1. XRD analysis

Fig. 3 presents XRD patterns of the developed Al-Si-Mg-Mn alloys with the various volume fraction of eutectic mixtures. The main XRD peaks were identified and they corresponded to α-Al, Si, Mg_2Si and α-AlFeMnSi phases. However, the small XRD peaks corresponded to π-AlFeMnMgSi phase.

3.2.2. Optical microstructure and EBSD analysis

Fig. 4 (a) shows a typical hypo-eutectic microstructure of alloy A in the as-cast state and the EBSD orientation map of alloy A is shown in Fig. 4 (b). From the optical micrograph, there are two types of eutectic at grain boundaries (further confirmed under SEM), which are named 'Eu1' and 'Eu2', and the volume fraction of eutectic mixture was determined to be 24 ± 8% from the image analysis. The microstructure of alloy B is shown in Fig. 4 (c), which is similar to alloy A. The volume fraction of eutectic mixture in alloy B is found to be 42 ± 7%, which is higher than that in alloy A. Alloy C exhibits a different microstructure compared with alloy A and alloy B, as shown in Fig. 4 (e). Apart from coarse eutectic and fine eutectic matrix labelled as 'EU1' and 'EU2', some coarse Mg_2Si and compact α-AlFeMnSi particles, were found with the size of 15–40 μm and 10–30 μm, respectively. The compositions of these phases measured by SEM-EDX are listed in Table 4. The as-cast microstructure of alloy C is dominated by eutectic structure and some α-Al grains were observed with the volume fraction of ~11%. The image analysis of α-Al volume fraction from the centre to edge in alloy C is shown in supplementary material (Fig. S1). The microstructure of eutectic Al-Si-Mg-Mn alloy has a bimodal morphology that consists of small rosette-like binary eutectic embedded within the fine quaternary eutectic matrix.

Two types of α-Al grains were observed, which are labelled as 'α1' and 'α2' in Fig. 4 (a,c). α1-Al phase shows coarse fragmented morphology in both alloy A and alloy B, separated by fine α2-Al grains. The α-Al grain size distribution of alloy A and alloy B analysed by the EBSD is

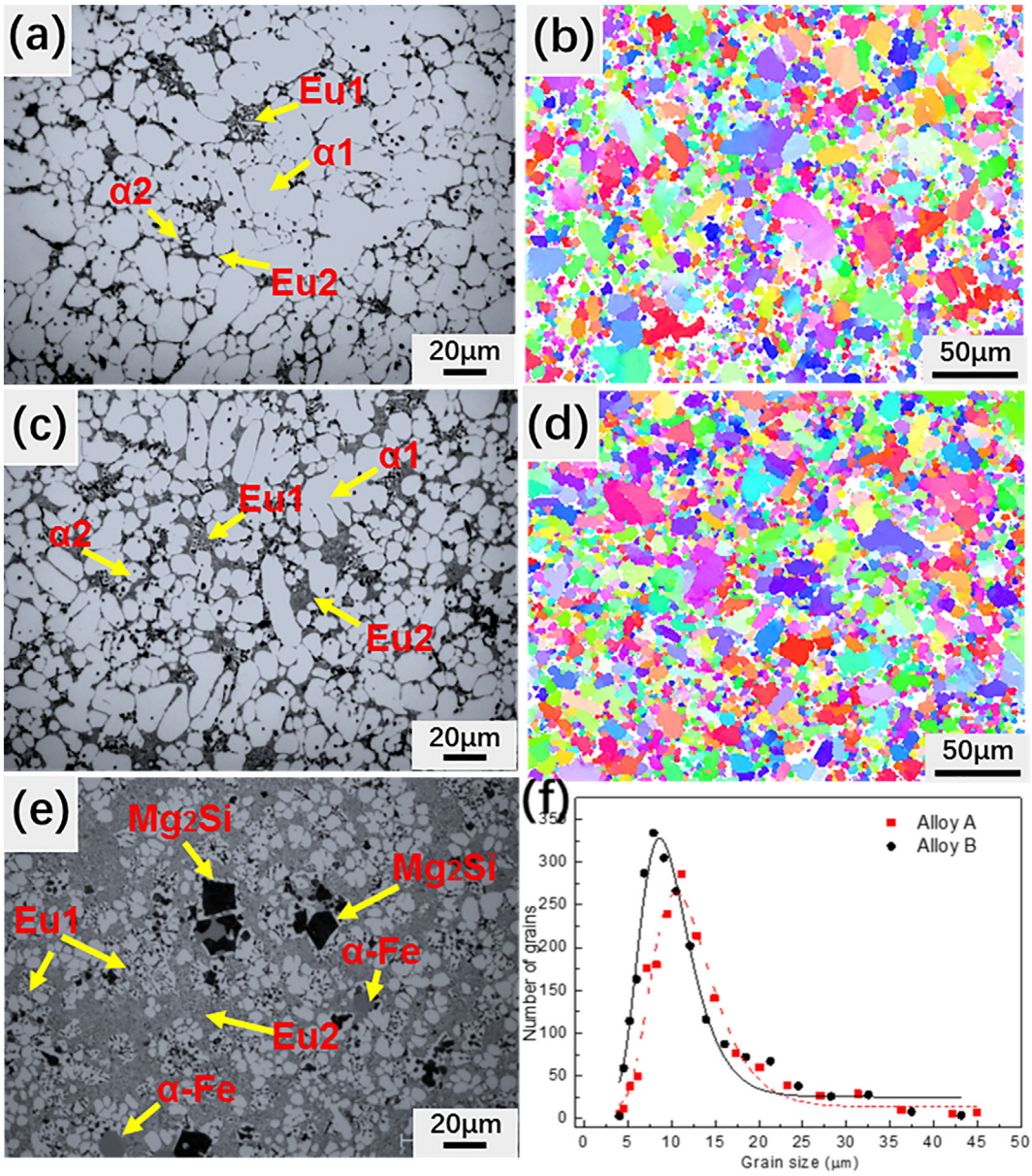

Fig. 4. Optical micrographs showing the microstructure evolution with the increased eutectic volume fraction in alloy A (a), alloy B (c) and alloy C (e); EBSD orientation map of alloy A (b), alloy B (d) and grain size distribution of alloy A and alloy B (f).

shown in Fig. 4 (b) and (d), respectively. The comparison of grain size distribution between alloy A and alloy B is shown in Fig. 4 (f). The average grain size of α2-Al and α1-Al are found to be 12 ± 5 μm and 35 ± 11 μm in alloy A and, 9 ± 4 μm and 30 ± 12 μm in alloy B, respectively.

3.2.3. DSC results

Fig. 5 shows typical DSC spectra of alloy A, alloy B and alloy C. From DSC curves obtained from a heating cycle, the onset temperature of the melting peak for each alloy was similar and was found to be 554 °C, which coincides with the calculated quaternary eutectic reaction temperature. There are two main endothermic DSC peaks for alloy A and alloy B, which correspond to the melting of the eutectic mixture and α-Al dendrites. However, only one endothermic DSC peak with a should feature was observed in alloy C. The shoulder feature is associated with the multiple eutectic reactions (e.g.binary and quaternary eutectic reaction) and the small volume fraction of α-Al dendrites. The DSC results validate the predicted solidification paths of these alloys with a various volume fraction of eutectic mixture. From the DSC curves obtained from the cooling cycle, two large exothermic peaks are found in alloy A and alloy B, which correspond to the formation of α-Al dendrites and eutectic mixture. However, there are some additional small exothermic peaks present in the DSC curves of these alloys as compared with those obtained from the heating cycle. It is because the cooling rate is very slow and the solidification occurs at near-equilibrium condition while the measured composition is slightly different from equilibrium composition. Thus some intermetallic compounds or ternary eutectic form before final eutectic reaction [17]. The alloy A has the highest solidification temperature of primary α-Al (611 °C), and the lowest temperature was found in alloy C.

3.2.4. Scanning electron microscopy results

The microstructure of eutectic mixture and α-AlFeMnSi particles was further characterised by SEM under backscattered electron imaging and in-lens mode, which are shown in Fig. 6 (a, c, e) and (b, d, f), respectively. Fig. 6 (a) and (c) are backscattered electron micrographs showing the microstructure of alloy A and alloy B, respectively. In Fig. 6. (a), the α-AlFeMnSi particles with size ranging from 1 to 3.5 μm were homogeneously distributed in alloy A. The area percentage of the α-AlFeMnSi particles is approximate 1.2%, which were analysed by ImageJ. In alloy B, the area percentage of α-AlFeMnSi particles is about 1.4% but they have a finer size of 1–2.5 μm and they are distributed within the eutectic region, as shown in Fig. 6. (c).

In alloy C, there is a small amount of fine α-AlFeMnSi particles present in the eutectic regions with a size of 1–2 μm, as shown in Fig. 6 (e) and (f). Large polygon Mg_2Si and compact α-AlFeMnSi particles with size over 10 μm were observed from EDX maps as shown in the supplementary material (Fig. S2). The average compositions of these intermetallic compounds were analysed and shown in Table 4. Fig. 6 (b) and (d) shows the eutectic microstructure in alloy A and alloy B under SEM in-lens mode taken at the same magnification. The 'EU1' and 'EU2' regions in alloy A show a finer microstructure compared with those in alloy B. The 'EU1' region has an interlamellar spacing of 0.3–0.7 μm, while in alloy B, the interlamellar spacing is 0.5–1.3 μm. The 'EU2' eutectic mixture in both alloy B and alloy A consist of four phases which are Si, Mg_2Si, and α-Al, together with needle-like π-AlFeMnSiMg phases [19]. The 'EU2' eutectic region in alloy C shown in Fig. 6 (f) is similar to that of alloy B. The 'EU2' eutectic region in alloy A shows a finer microstructure. It can be noticed in Fig. 6 (b) that, apart from three types of phases (i.e. Si, Mg_2Si and α-Al), the needle-like π-AlFeMnSiMg phase with higher area fraction was found in the ultrafine eutectic region in alloy A having a width of 100–400 nm and length of 2–5 μm. Further characterisation of the ultrafine eutectic regions with TEM will be discussed later.

The aspect ratio and average size of eutectic Si phase in 'EU2' are shown in Table 5, which were characterised using in-lens SEM images (not shown here), taken at higher magnification. It can be found that

Table 4
Average compositions of intermetallic phases characterised by SEM EDX analysis.

Alloy name	Morphology	Identified compound	Al	Si	Mg	Mn	Fe
			at.%				
Alloy A	Fine compact	$Al_{15}(Fe,Mn)_3Si_2$	72.6	11.1	–	13.6	2.7
Alloy B	Fine compact	$Al_{15}(Fe,Mn)_3Si_2$	73.1	10.9	–	12.3	3.7
Alloy C	Coarse compact	$Al_{15}(Fe,Mn)_3Si_2$	71.5	12	–	12.9	3.6
	polygon	Mg_2Si	81.7	5.8	12.5	–	–
	Fine compact	$Al_{15}(Fe,Mn)_3Si_2$	71.7	11.7	–	12.9	3.7

the Si in these alloys has nearly the same aspect ratio. In addition, the Si particles present in alloy A has the smallest average size of 0.23 ± 0.14 μm as compared to those present in alloy B with the largest average size of 0.42 ± 0.28 μm. Moreover, the finer eutectic Si phase was achieved in the current Al-Si-Mg-Mn alloys, compared with binary Al—Si eutectic alloys with a similar solidification condition [20–22].

The size distributions of α-AlFeMnSi particle present in alloy A, alloy B and alloy C are shown in Fig. 7 (a,b,c), respectively. Alloy B and alloy C have finer particles which have a concentrated size range between 1 and 1.5 μm, while the much broader distribution of α-AlFeMnSi particles appears in alloy A. There are a few large α-AlFeMnSi particles (over 10 μm) in alloy C with hexagonal morphology. The inserted images are backscattered electron micrographs taken at low magnification showing the size and distribution of α-AlFeMnSi particles. Furthermore, the aspect ratio of α-AlFeMnSi particles was analysed in Fig. 7 (d). The α-Fe particles present in alloy B and alloy C show a lower aspect ratio.

3.2.5. Transmission electron microscopy results

Fig. 8 (a) shows a bright-field TEM micrograph of the quaternary eutectic mixture present in alloy A taken at [010] zone axis of π-AlFeMnSiMg phase, together with corresponding selected area diffraction patterns (SADP), as shown in Fig. 8 (d-g). Fig. 8 (b) shows BF-STEM image and elemental distributions of ultrafine eutectic regions. There are four kinds of phases co-existed within the ultrafine eutectic region of alloy A, which coincide with the microstructure characterised under SEM. Mg_2Si phase has a size of ~100 nm while π-AlFeMnSiMg phase has ~250 nm width and 2–3 μm length. The Si phase in alloy A exhibits fragmented and spheroidized morphology. Moreover, the high density of twins was observed in some Si particles, together with the corresponding SADP pattern, as shown in Fig. 8 (g). It is reported that the induced twinning in Si by the additional element or impurities is the most established growth model [23]. Herein, the high density of twinning Si may result from the absorption of the additional elements

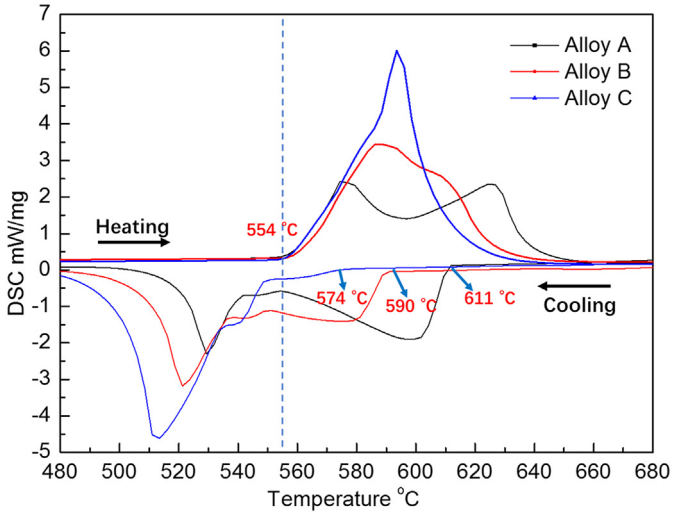

Fig. 5. DSC curves of alloy A, alloy B and Alloy C obtained from both heating and cooling with a rate of 10 K/min.

of Mg, Fe or Mn preventing further growth. The Mg_2Si phase has ultrafine particulate morphology with the size of 100–250 nm which is usually observed to be Chinese-script morphology in other solidification conditions with a lower cooling rate [24]. Fig. 8 (c) and (e) show the EDS spectra, together with an inset of measured composition and SADP of π-AlFeMnSiMg phase, respectively. The substitution of Mn in π-AlFeMnSiMg phase was found as well as lower content of Fe and Mn compared with the equilibrium π-AlFeMnSiMg phase.

3.3. Mechanical properties

Fig. 9 (a) shows tensile stress-strain curves of these Al-Si-Mg-Mn alloys prepared by HPDC. These alloys have a yield strength above 230 MPa. However, the elongation to fracture increases with decreasing volume fraction of eutectic mixture. Fig. 9 (b) shows the comparison of the tensile properties of these three Al-Si-Mg alloys. Alloy A has the highest elongation to fracture of 4.3% and yield strength of 231 MPa. The excellent yield strength of 281 MPa was achieved in alloy B with reasonable elongation to fracture of 2.3%. Although alloy C has the highest yield strength of 285 MPa, its elongation to fracture is only limited to 0.8%. The yield strength of current Al-Si-Mg alloys is much higher than those of commercially available diecast aluminium alloys (Table 1), while the elongations of alloy A and alloy B are at the acceptable level. It should be noticed that no extra elements such as Cu and Zn were added as strengthening elements to design the alloy with improved high yield strength.

Fig. 10 shows the fracture surface of alloy A (a) and alloy B (c), which were taken in the middle part of the sample. The fracture is a combination of eutectic region separation and cleavage fracture of α1-Al grains. It should be noted that the fracture surface was dominated by the eutectic separation, and only a few fractures of α1-Al grains were observed. The separation of the eutectic regions at grain boundaries of alloy A and alloy B were shown in Fig. 10 (b) and (d), respectively. The cracks were found in large Mg_2Si in alloy C shown in Fig. 10 (e) and it shows cleavage features. It can be noted that the cracks initiated from large polygon Mg_2Si particles, leading to the low ductility in alloy C.

Fig. 11 shows the dislocation pile-ups at the boundary between eutectic and α-Al grain after 3% interrupted tensile testing of alloy A. The

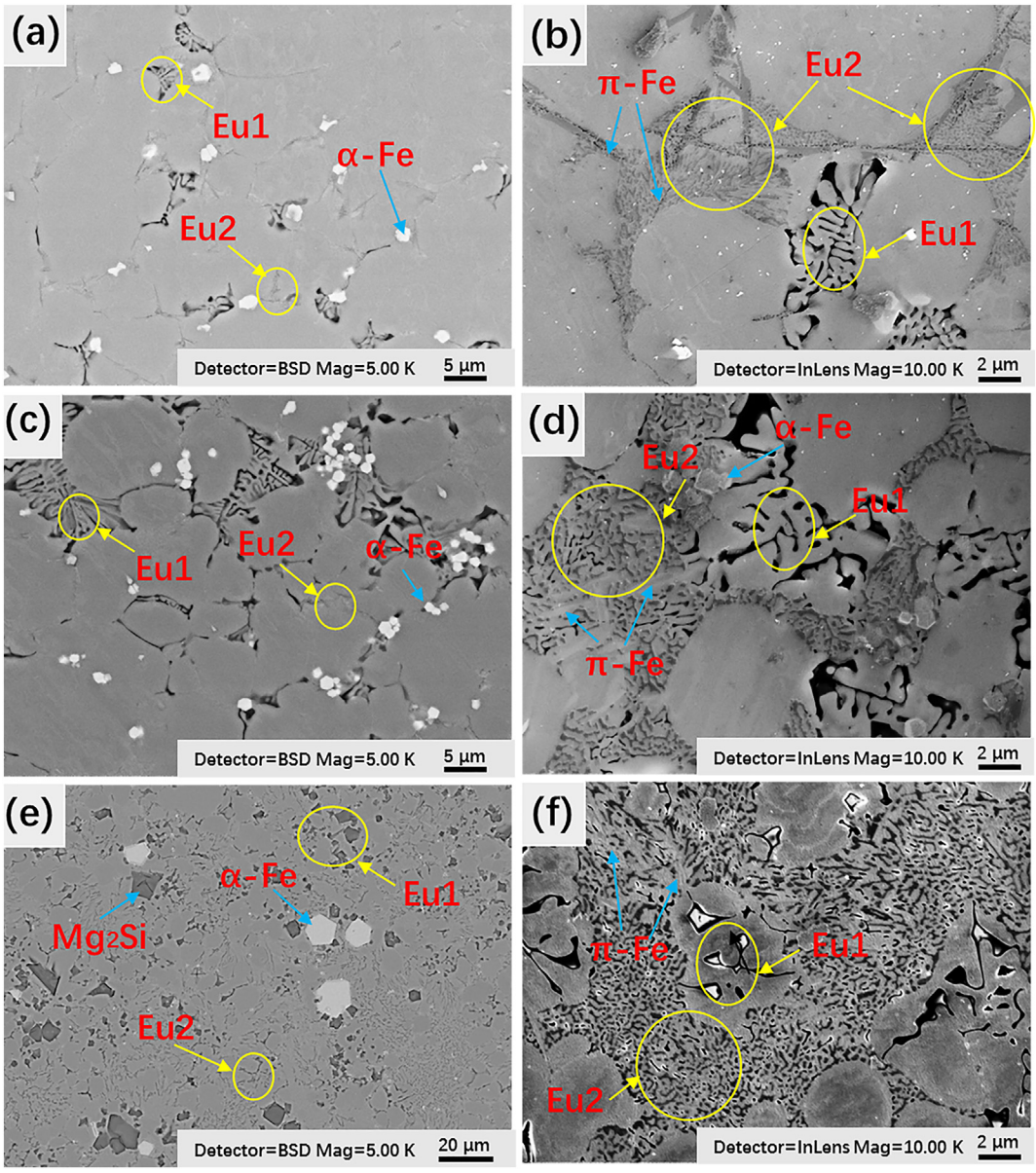

Fig. 6. (a, c, e) Backscattered SEM micrographs showing the microstructure of alloy A, alloy B alloy C (b, d, f) in-lens SEM micrographs with larger magnification showing the eutectic region in alloy A, alloy B and alloy C.

Table 5
Aspect ratio and equivalent diameter of Si particles in alloy A, alloy B and alloy C.

Alloy	Alloy A	Alloy B	Alloy C
Si aspect ratio	2.55 ± 2.02	2.44 ± 1.37	2.43 ± 1.59
Si average diameter (μm)	0.23 ± 0.14	0.42 ± 0.28	0.38 ± 0.15

strain contrast inside α-Al grains indicates massive dislocation pile-ups at the boundary which results from plastic deformation. More dislocations were found at the boundary of the ultrafine quaternary eutectic region shown in Fig. 11 (b).

4. Discussion

4.1. Microstructure evolution

The HPDC process is a two-stage solidification process, where some phases partially solidified in the shot sleeve at a very slow cooling rate and rest of liquid solidified in the die cavity at a very high cooling rate [25]. Hence, two types of α-Al phases were observed in alloy A and alloy B, and α1-Al solidified in the shot sleeve has a larger size, while much finer α2-Al forms in the die cavity. It can be found that increasing the volume fraction of the eutectic mixture can contribute to a decrease of α2-Al and α1-Al grains in size. The refined α-Al grain size with the increasing volume fraction of eutectic is due to the growth restriction mechanism [26]. The more addition of Si and Mg into the alloys increases the volume fraction of eutectic and in the meantime, more solutes segregate at the solid/liquid interface, affecting the constitutional undercooling and restricting the growth of dendrites. Therefore, the finer α-Al grain size was achieved. Moreover, in alloy C, large polygon Mg_2Si and compact α-AlFeMnSi particles are formed without the presence of coarse α1-Al phase. From Pandat 8.5 prediction, some intermetallic compounds formed before the eutectic reactions. It should also be noted that alloy C is close to the ternary eutectic composition, which is reported to be a quasi-binary reaction and L → α-Al + Mg_2Si forms before final eutectic reaction [27]. As a result, coarse compact α-AlFeMnSi particles and some eutectic phase of polygon Mg_2Si formed in the shot sleeve. In addition, some α2-Al phases were found in the sample with an average volume fraction of 11% from edge to centre, although the composition in alloy C is close to eutectic composition. It is because HPDC process is nonequilibrium process with two-stage solidification. Large Mg_2Si and α-AlFeMnSi form in the shot sleeve, consuming the solute and the composition on the later solidification in die cavity is changed. Furthermore, segregation of solute distribution exists that near the surface or defect band there is an increase of solute concentration [28]. Consequently, the composition is close to off-eutectic composition and some α2-Al dendrites form.

The fine eutectic morphology solidified in the die cavity with submicron-scale binary eutectic and ultrafine quaternary eutectic is achieved in the Al-Si-Mg-Mn eutectic or hypo-eutectic alloys by HPDC process. The bimodal eutectic microstructure of eutectic alloys was also found and reported by Kim et al. [14]. The typical bimodal eutectic microstructure in eutectic alloys consists of two types of eutectic with different length scale and the formation of this unique structure is due to the high cooling rate and additional elements which can affect the topological and crystallographic anisotropy of the liquid/solid interface, and destabilize the liquid/solid interface, resulting in shifting the couple eutectic growth zone under nonequilibrium solidification condition [29]. Thus, the homogeneous distribution of inhomogeneous structure formed in ternary eutectic alloys. Furthermore, from XRD results, the change of volume fraction of eutectic mixture has no influence on the types of phases in the microstructure. It should be noted that π-

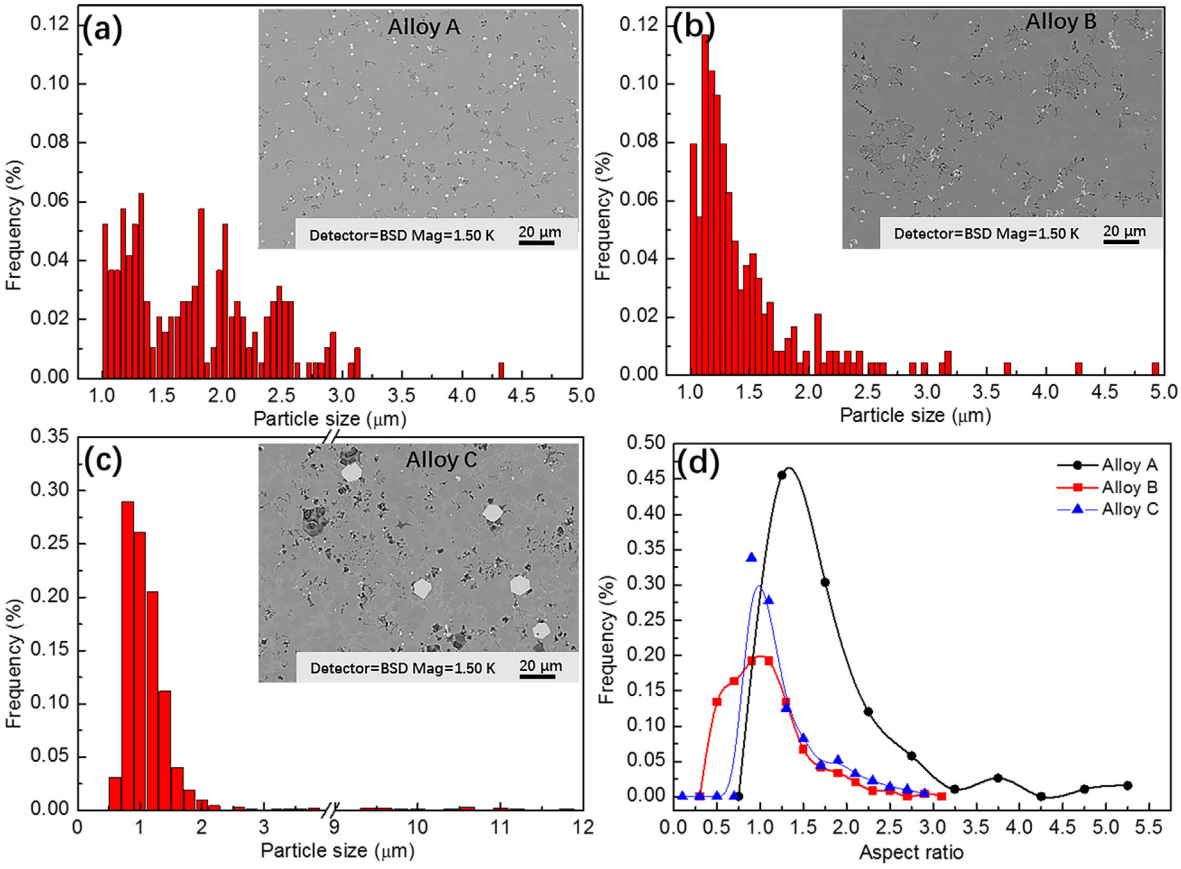

Fig. 7. The size distribution of α-AlFeMnSi particles present in alloy A (a), alloy B (b) and alloy C (c) together with insets of SEM micrographs of corresponding alloys and (d) the frequency of the aspect ratio.

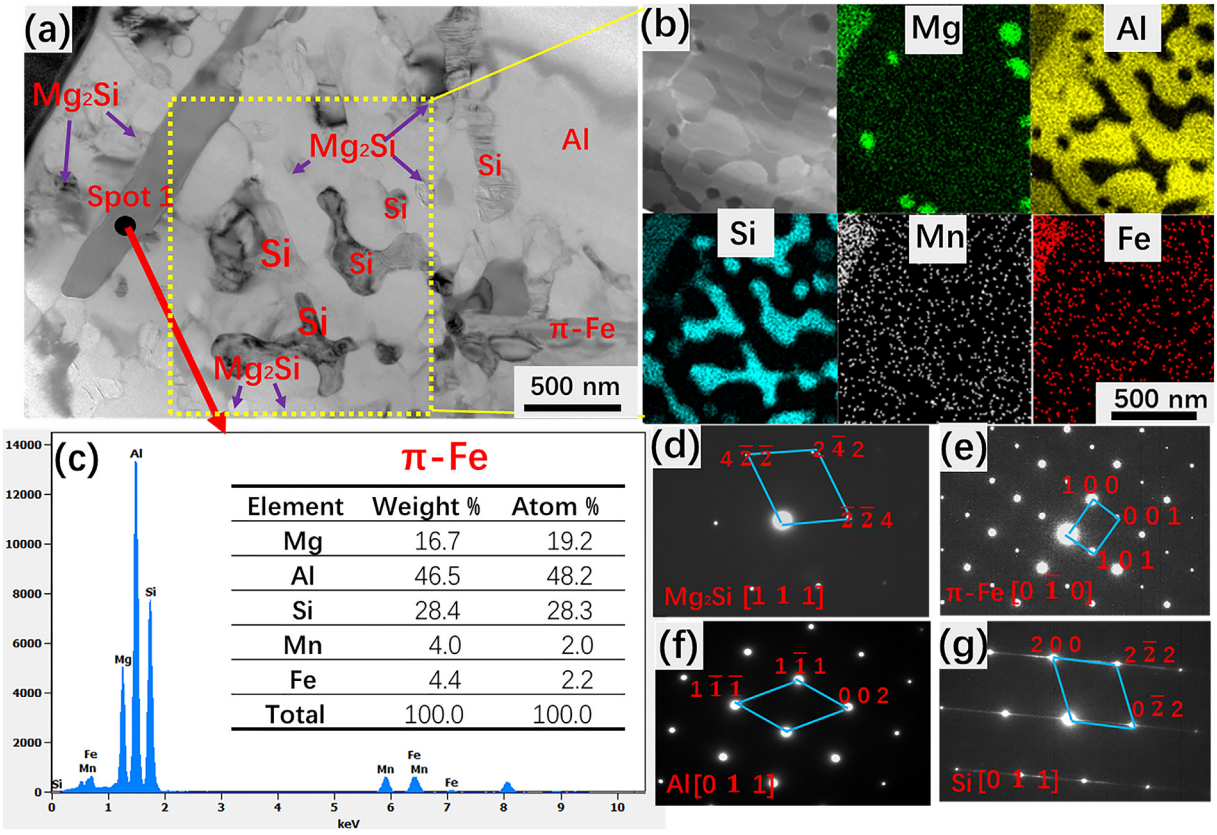

Fig. 8. (a) Bright-field TEM micrograph of the ultrafine eutectic region in alloy A showing the microstructure of quaternary eutectic (b) the elemental distributions inside the eutectic region (c) EDS spectra of π-AlFeMnSiMg phase, together with inset of measured composition and (d-g) SADP pattern of π-AlFeMnSiMg, Si, Mg_2Si and α-Al phases, respectively.

AlFeMnSiMg appeared in these alloys which was not predicted by Pandat 8.5. It is mainly due to the non-equilibrium solidification under HPDC process and the database employed in the current study. The eutectic structure is finer than some binary Al—Si diecast alloys. It is because the multicomponent recipe in the final solidification liquid can increase the constitutional undercooling and contribute to competitive growth of multi-phase, resulting in the refinement of the eutectic phase [17,30]. Moreover, The eutectic Si phase in alloy A is most exceptional among these three alloys. Compared with alloy B and alloy C, 'EU2' in alloy A has the smallest interdendritic regions (eutectic regions), indicating less remaining liquid and more solid/liquid interfaces. Therefore much fastest heat transfer through α-Al dendrites during final eutectic solidification was obtained. As a result, 'EU2' has the smallest size of Si.

The addition of Mn can suppress the formation of β-Fe phase in HPDC, and similar to the development of α-Al phases, the dual size distributions of α-AlFeMnSi particles are caused by two-stage solidification as well. It was reported that the coarse α-AlFeMnSi particles solidified in the shot sleeve are below 10 μm, provided the iron content is less 0.2% [9]. Compared with alloy A, alloy B has the finer α-AlFeMnSi particles with a lower aspect ratio and the size of α-AlFeMnSi particles is below 5 μm in all these three alloys. According to the solidification sequence predicted by Pandat 8.5 in Fig. 2, the majority of α-AlFeMnSi particles formed at a temperature ranging from 617 to 600 °C before α-Al formation in alloy B, while in alloy A the formation of α-AlFeMnSi particles accompanies with α-Al at the temperature ranging from 620 °C to 556 °C. Therefore, the α-AlFeMnSi particles in alloy B have less solidification time due to increased undercooling. As a result, α-AlFeMnSi particles

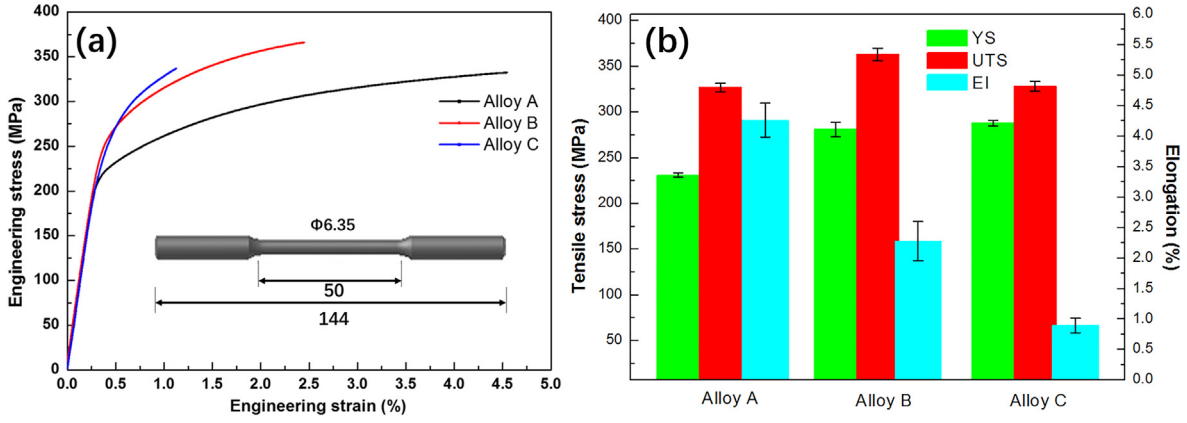

Fig. 9. Mechanical properties of the as-cast Al-Si-Mg-Mn alloys (a) tensile stress-strain curves, (b) average tensile properties.

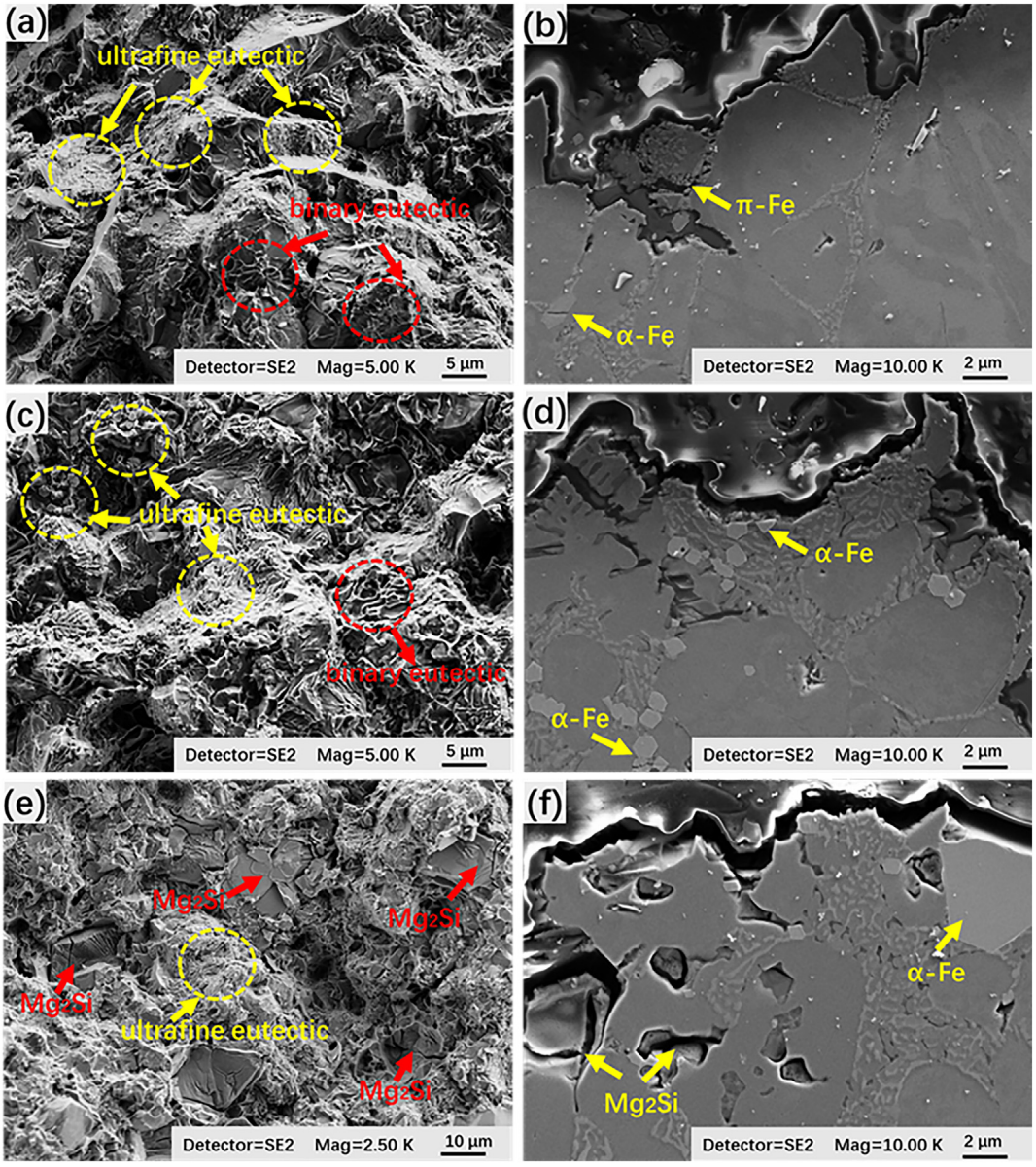

Fig. 10. SEM micrographs of specimens after tensile tests, showing fractured surface of alloy A (a), alloy B (c) and alloy C (e); and crack propagation through the eutectic structure of alloy A (b), alloy B (d) and alloy C (f) (note: loading axes for (b), (d) and (f) are vertical).

in alloy B shows faceted hexagonal morphology with a lower aspect ratio and finer size distribution. They are distributed along grain boundaries or inside the eutectic regions. Furthermore, it can bœe observed that a large area fraction of large α-AlFeMnSi particles formed in alloy C, and finer α-AlFeMnSi particles formed at the eutectic regions with lower area fraction. The solidification path of alloy C involves the

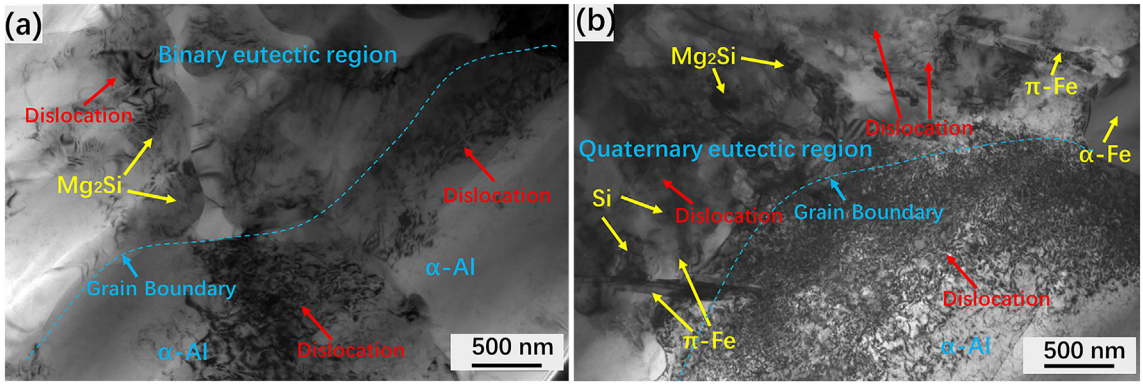

Fig. 11. TEM BF micrographs showing dislocations at the binary eutectic region (a) and the ultrafine quaternary eutectic region (b) of 3%-tensile-strained alloy A.

formation of α-AlFeMnSi particles from 615 °C to 554 °C, prior to eutectic reaction, according to Fig. 2. Herein, the large α-AlFeMnSi particles nucleated and grew in the short sleeve. This implies a reduced amount of Fe present in the remaining liquid and it solidifies into few finer α-AlFeMnSi particles near the final eutectic temperature.

The π-AlFeMnSiMg phase in alloy A is much finer compared with those in A356 and A357 alloys [18,31]. In alloy A, the formation of final quaternary eutectic reaction with a high volume fraction of refined π-AlFeMnSiMg phase is attributed to the partitioning of Fe to the remaining liquid and much faster heat transfer of the last smaller interdendritic regions under non-equilibrium solidification condition [18]. Lastly, the composition of π-AlFeMnSiMg phase is slightly different from the equilibrium composition $Al_9FeMg_3Si_5$ taking into consideration of substitution of Mn, and this results from non-equilibrium solidification process.

4.2. Relationship between microstructure and mechanical properties

The Al-Si-Mg-Mn alloys in the current work showed excellent mechanical properties, especially having a high yield strength in excess of 200 MPa. The mechanical properties of the dendrite-ultrafine eutectic composite strongly depend on the phase selection and volume fraction of strengthening phases [13]. In another word, the elongation can be tailored by controlling the volume fraction of eutectic mixture, and at the same time, the strength can be improved via optimisation of eutectic microstructure from monolithic eutectic structure to multimodal eutectic structure with multicomponent phase. The microstructure of currently developed alloys consists of the soft α-Al primary phase, ultrafine/submicron-scale eutectic mixture, and small α-AlFeMnSi phases. The soft α-Al primary phase can act as a barrier for the crack propagation of catastrophic failure. The ultrafine/submicron-scale eutectic structure and fine iron-contained particles contribute to the high strength for these alloys. The elongation of the alloys was dominated by the volume fraction of eutectic mixture present in these alloys. Hence, the highest elongation was achieved in alloy A. However, the presence of large brittle Mg_2Si or large α-AlFeMnSi phases, together with the highest volume fraction of eutectic mixture present in alloy C is responsible for the lowest elongation to fracture of ~0.8%.

The coarse Si particles in binary Al—Si diecast alloys playing an important role in the strength as they are the main sources of stress concentration and the crack paths preferentially go through the eutectic region. In the current work, ultrafine Si and Mg_2Si phases together with fine iron-contain multicomponent phases inside the eutectic region can be more effective to suppress the crack development and α-AlFeMnSi particles formed at the grain boundary further improve the tensile stress. Moreover, based on Hall-Petch theory, higher yield strength can be achieved with much finer eutectic structure [32]. In addition, the ultrafine quaternary eutectic with much finer structure is more effective to inhibit the propagation of dislocation, as shown in Fig. 11. Some irregular dislocations were found inside the eutectic regions as well, due to the generation of dislocations within the eutectic region. No cracks were found on the eutectic phases. Therefore, the plastic deformation of ultrafine eutectic alloys was governed by dislocation slip inside the α-Al grains and the excellent yield strength is because of the interaction of dislocations between ultrafine eutectic and α-Al grains leading to better work hardening regime [33]. Hence, the alloys in the current study have higher strength than some other diecast aluminium alloys. It should also be noted that alloy B has higher strength than alloy A, due to much higher volume fraction of eutectic mixture. However, the highest volume fraction was obtained in alloy C, and the yield strength is similar to alloy B. The reasons are as follows. Firstly, in alloy C, a lot of coarse Mg_2Si phases which form from binary eutectic reaction. This reduces the contribution of binary eutectic in the strength compared with that in alloy A and alloy B which have much finer binary eutectic lamellar spacings. Secondly, a large volume fraction of large compact α-AlFeMnSi phases formed prior to the final eutectic reaction in alloy C, resulting in a small quantity of fine α-AlFeMnSi phases forming in the die cavity. Therefore, the strength of alloy C is balanced by the increased volume fraction of eutectic mixtures and coarsening of α-AlFeMnSi and Mg_2Si phases. Consequently, alloy C exhibits similar yield strength with alloy B.

5. Conclusion

(1) High strength die-cast aluminium alloys have been developed based on the concept of multi-component ultrafine secondary phase strengthening mechanism. The as-cast Al-Si-Mg-Mn alloy with 30% eutectic provides the high yield strength of 231 MPa, ultimate tensile strength of 340 MPa and elongation of 4.3%. The as-cast Al-Si-Mg-Mn alloy with 50% eutectic exhibits the super high yield strength of 281 MPa and elongation of 2.3%.
(2) The high strength die-cast Al-Si-Mg-Mn alloys show complex microstructure, consisting of primary α-Al phase, α-AlFeMnSi, binary eutectic (Al + Mg_2Si) and ultrafine quaternary Al + Mg_2Si + Si + π-AlFeMnSiMg eutectic.
(3) The finest eutectic Si phase with an average size of 230 nm was achieved in the Al-Si-Mg-Mn die-cast alloy with 30% eutectic mixture. The fine α-AlFeMnSi particles in Al-Si-Mg-Mn hypoeutectic alloys were obtained with an average size below 2 μm.
(4) The high number of dislocation pile-ups at eutectic boundaries or inside the eutectic cause excellent yield strength.

CRediT authorship contribution statement

Qing Cai: Conceptualization, Methodology, Investigation, Writing - original draft, Writing - review & editing. **Chamini L. Mendis:** Formal analysis, Investigation, Methodology, Writing - review & editing. **Isaac T.H. Chang:** Conceptualization, Writing - review & editing, Supervision. **Zhongyun Fan:** Methodology, Investigation.

Declaration of competing interest

The authors declare no competing interests for the manuscript "Microstructure evolution and mechanical properties of new die-cast Al-Si-Mg-Mn alloys" submitted to *Materials & Design*.

Acknowledgements

This work was supported by the Engineering and Physical Sciences Research Council (EPSRC) under Future Liquid Metall Engineering Hub (LIME hub) (EP/N007638/1). The authors would like to thank Experimental Techniques Centre Brunel University London for the access to microstructure characterisation facilities. Besides, Qing Cai would like to thank Brunel University London for the financial support towards his PhD studentship.

Data availability

The raw/processed data required to reproduce these findings cannot be shared at this time as the data also forms part of an ongoing study.

Appendix A. Supplementary data

Supplementary data to this article can be found online at https://doi.org/10.1016/j.matdes.2019.108394.

References

[1] F. Bonollo, N. Gramegna, G. Timelli, High-pressure die-casting: contradictions and challenges, JOM 67 (2015) 901–908.
[2] J. Rowe, Advanced Materials in Automotive Engineering, Woodhead Publishing Limited, 2012.

[3] L. Wang, M. Makhlouf, D. Apelian, Aluminium die casting alloys: alloy composition, microstructure, and properties-performance relationships, Int. Mater. Rev. 40 (1995) 221–238.
[4] P. Zhang, Z. Li, B. Liu, W. Ding, L. Peng, Improved tensile properties of a new aluminium alloy for high pressure die casting, Mater. Sci. Eng. A 651 (2016) 376–390.
[5] X. Dong, H. Yang, X. Zhu, S. Ji, High strength and ductility aluminium alloy processed by high pressure die casting, J. Alloys Compd. 773 (2019) 86–96.
[6] S. Ji, F. Yan, Z. Fan, Development of a high strength Al–Mg2Si–Mg–Zn based alloy for high pressure die casting, Mater. Sci. Eng. A 626 (2015) 165–174.
[7] L. Wang, P. Turnley, G. Savage, Gas content in high pressure die castings, J. Mater. Process. Technol. 211 (2011) 1510–1515.
[8] S. Ji, W. Yang, F. Gao, D. Watson, Z. Fan, Effect of iron on the microstructure and mechanical property of Al–Mg–Si–Mn and Al–Mg–Si diecast alloys, Mater. Sci. Eng. A 564 (2013) 130–139.
[9] M.C. Reboul, B. Baroux, Metallurgical aspects of corrosion resistance of aluminium alloys, Mater. Corros. 62 (2011) 215–233.
[10] T.D. Burleigh, E. Ludwiczak, R.A. Petri, Intergranular corrosion of an aluminum-magnesium-silicon-copper alloy, CORROSION 51 (1995) 50–55.
[11] F. D'Elia, C. Ravindran, Influence of grain refinement on hot tearing in B206 and A319 aluminum alloys, Trans. Indian Inst. Met, Springer-Verlag 2009, pp. 315–319.
[12] B.B. Sun, M.L. Sui, Y.M. Wang, G. He, J. Eckert, E. Ma, Ultrafine composite microstructure in a bulk Ti alloy for high strength, strain hardening and tensile ductility, Acta Mater. 54 (2006) 1349–1357.
[13] I.V. Okulov, M. Bönisch, A.S. Volegov, H.S. Shahabi, H. Wendrock, T. Gemming, J. Eckert, Micro-to-nano-scale deformation mechanism of a Ti-based dendritic-ultrafine eutectic alloy exhibiting large tensile ductility, Mater. Sci. Eng. A 682 (2017) 673–678.
[14] J.T. Kim, S.W. Lee, S.H. Hong, H.J. Park, J.Y. Park, N. Lee, Y. Seo, W.M. Wang, J.M. Park, K.B. Kim, Understanding the relationship between microstructure and mechanical properties of Al-Cu-Si ultrafine eutectic composites, Mater. Des. 92 (2016) 1038–1045.
[15] Annual Book of ASTM Standards. 02.02, , ASTM, Warrendale PA, 1993.
[16] D.M. Stefanscu, J.R. Davis, J.D. Destefani (Eds.), ASM Metals Handbook, ninth ed., vol. 15, ASM International, Casting, Metals Park, OH, 1998.
[17] Z. Lu, L. Zhang, Thermodynamic description of the quaternary Al-Si-Mg-Sc system and its application to the design of novel Sc-additional A356 alloys, Mater. Des. 116 (2017) 427–437.
[18] C.R. Barbosa, G.H. Machado, H.M. Azevedo, F.S. Rocha, J.C. Filho, A.A. Pereira, O.L. Rocha, Tailoring of processing parameters, dendritic microstructure, Si/intermetallic particles and microhardness in as-cast and heat-treated samples of Al7Si0.3Mg alloy, Met. Mater. Int. (2019) 1–14.
[19] C.R. Barbosa, J.O.M. de Lima, G.M.H. Machado, H.A.M. de Azevedo, F.S. Rocha, A.S. Barros, O.F.L. da Rocha, Relationship between aluminum-rich/intermetallic phases and microhardness of a horizontally solidified AlSiMgFe alloy, Mater. Res. 22 (2018).
[20] K.-T. Chiang, N.-M. Liu, T.-C. Tsai, Modeling and analysis of the effects of processing parameters on the performance characteristics in the high pressure die casting process of Al–Si alloys, Int. J. Adv. Manuf. Technol. 41 (2009) 1076–1084.
[21] X. Dong, X. Zhu, S. Ji, Effect of super vacuum assisted high pressure die casting on the repeatability of mechanical properties of Al-Si-Mg-Mn die-cast alloys, J. Mater. Process. Technol. 266 (2019) 105–113.
[22] G. Timelli, A. Fabrizi, The effects of microstructure heterogeneities and casting defects on the mechanical properties of high-pressure die-cast AlSi9Cu3(Fe) alloys, Metall. Mater. Trans. A Phys. Metall. Mater. Sci. 45 (2014) 5486–5498.
[23] J.H. Li, M. Albu, F. Hofer, P. Schumacher, Solute adsorption and entrapment during eutectic Si growth in A-Si-based alloys, Acta Mater. 83 (2015) 187–202.
[24] Y.L. Liu, S.B. Kang, H.W. Kim, The complex microstructures in an as-cast Al-Mg-Si alloy, Mater. Lett. 41 (1999) 267–272.
[25] W. bo Yu, S. Liang, Y. you Cao, X. bo Li, Z. Peng Guo, S. mei Xiong, Interfacial heat transfer behaviour at metal/die in finger-plated casting during high pressure die casting process, China Foundry 14 (2017) 258–264.
[26] A.M. Mitrašinović, F.C. Robles Hernández, Determination of the growth restriction factor and grain size for aluminium alloys by a quasi-binary equivalent method, Mater. Sci. Eng. A 540 (2012) 63–69.
[27] Y. Kaygisiz, N. Maraşli, Microstructural, mechanical and electrical characterization of directionally solidified Al-Si-Mg eutectic alloy, J. Alloys Compd. 618 (2015) 197–203.
[28] S. Ji, Y. Wang, D. Watson, Z. Fan, Microstructural evolution and solidification behavior of Al-Mg-Si alloy in high-pressure die casting, Metall. Mater. Trans. A. 44 (2013) 3185–3197.
[29] J.M. Park, N. Mattern, U. Kühn, J. Eckert, K.B. Kim, W.T. Kim, K. Chattopadhyay, D.H. Kim, High-strength bulk Al-based bimodal ultrafine eutectic composite with enhanced plasticity, J. Mater. Res. 24 (2011) 2605–2609.
[30] H. Eckert, G. He, J. Das, W. Loser, Nanostructured composites in multicomponent alloy systems, Mater. Trans. 44 (2003) 1999–2006.
[31] R. Chen, Q. Xu, H. Guo, Z. Xia, Q. Wu, B. Liu, Correlation of solidification microstructure refining scale, Mg composition and heat treatment conditions with mechanical properties in Al-7Si-mg cast aluminium alloys, Mater. Sci. Eng. A 685 (2017) 391–402.
[32] B. Gwalani, S. Gorsse, D. Choudhuri, Y. Zheng, R.S. Mishra, R. Banerjee, Tensile yield strength of a single bulk Al 0.3 CoCrFeNi high entropy alloy can be tuned from 160 MPa to 1800 MPa, Scr. Mater. 162 (2019) 18–23.
[33] L.M. Kang, C. Yang, Y.J. Zhao, X.X. Li, S.G. Qu, W.W. Zhang, Y. Long, Z.Y. Xiao, Bimodal eutectic titanium alloys: microstructure evolution, mechanical behaviour and strengthening mechanism, Mater. Sci. Eng. A 700 (2017) 10–18.